Analysis of traveling-wave electro-osmotic pumping with double-sided electrode arrays

Hung-Chun Yeh,[1] Ruey-Jen Yang,[1,*] and Win-Jet Luo[2,†]

[1]*Department of Engineering Science, National Cheng Kung University, Tainan 701, Taiwan*

[2]*Department of Refrigeration, Air Conditioning and Energy Engineering, National Chin-Yi University of Technology,*
Taiping City, Taichung County 411, Taiwan

In this paper, a series of numerical simulations was performed to investigate the pumping performance of electro-osmotic micropumps containing electrode arrays patterned on the upper and lower sides of a microchannel. The simulations have been analyzed with a linear electro-osmotic model based upon the Debye-Hückel theory of the double layer. The potential drop across the diffuse layer is assumed to be less than 25 mV ($k_B T/e$), and there is a linear response between the surface charge and the voltage drop across the double layer. The double layer is not resolved but is lumped into effective parameters that are imported from the Debye-Hückel and Stern layers. We examined the effects of the relative positioning of the electrodes in the opposing arrays (i.e., symmetrical or staggered), and the phase lag and the angular frequency of the alternating current (ac) signals applied to the electrodes within the two arrays. A critical height of the microchannel was observed, below which the interactions of the applied electrical potentials on the walls became significant. The optimum pumping effect was obtained when the electrode arrays were symmetrical to one another around the centerline of the channel and were activated by ac potentials with a $0°$ phase shift. The corresponding angular frequency of the maximum pumping velocity for different phase shifts of the applied ac signals was also determined. Overall, the simulation results presented in this paper provide a useful insight into the optimal design parameters and operating conditions for micropumps containing two arrays of microelectrodes on the microchannel walls.

PACS number(s): 47.61.Fg, 47.65.−d, 85.85.+j

I. INTRODUCTION

There has been a recent surge in studies exploring micropump technologies, motivated, in part, by the need to develop pumping mechanisms for biological fluid handling, such as for polymerase chain reactions and lab-on-a-chip and micrototal analysis systems (μTASs). Lab-on-a-chip devices and μTASs require the precise control and manipulation of tiny volumes of fluid in small channels [1]. Many techniques have been developed to pump liquids in microdevices, which can broadly be classified into two main categories. (1) Mechanical displacement micropumps exert oscillatory or rotational pressure forces on the working fluid through a moving solid-fluid. Examples of these pumps include vibrating diaphragm pumps [2,3], peristaltic pumps [4–6], rotary pumps [7–9], or fluid-fluid boundary pumps, including ferrofluid, phase change, or gas permeation pumps. (2) Electro- and magnetokinetic micropumps provide direct energy transfer to pumping power and generate flows due to the continuous addition of energy. Examples of these pumps include electro-osmosis pumps [10], electrowetting pumps [11], thermocapillary pumps [12], electrohydrodynamic (EHD) pumps [13], and alternating current (ac) electro-osmosis pumps. Pumps based on EHD methods in which an electrical force applied directly to the liquid provides the pumping effect without any moving mechanical parts have gained particular attention due to their implicit simplicity, low cost, ease of fabrication, and potential for integration with other microfluidic devices.

The recent interest in ac electrokinetic micropumps stems from experimental observations by Green *et al.* [14] concerning fluid motion induced by ac electro-osmosis over pairs of microelectrodes [15,16] and by a theoretical prediction by Ajdari [17] that the same mechanism would generate an ac electro-osmosis pumping effect by utilizing electrode arrays with various asymmetric configurations. Studer and co-workers demonstrated the experimental pumping of an electrolyte with a low-voltage ac-biased electrode array, and soon after, the same effect was reported by a number of other groups who observed flow velocity on the order of millimeters per second [18–26]. Several theoretical models have been proposed in parallel with the experimental observations [27–29]. Two principal techniques have emerged for microfluidic flows driven using coplanar electrode arrays: asymmetric electrode pairs subjected to a common ac signal [22,26] and arrays of electrodes of equal width subjected to a traveling-wave potential with four phases [23–25]. Of these two techniques, García-Sánchez *et al.* [25] demonstrated that the traveling-wave electro-osmotic (TWEO) method is more efficient because it achieves a microfluidic flow of higher velocity and uses a lower applied voltage. However, the optimum design of the microelectrode structure is still a matter of debate [30].

EHD pumping also employs a traveling-wave signal. TWEO pumping occurs because of electrical forces on the induced charge in the diffuse double layer, while EHD pumping occurs because of electrical forces on induced charges that appear in the liquid bulk due to gradients of conductivity and permittivity [31,32]. A traveling-wave electrode array is also used to induce the dielectrophoretic motion of particles [33–35].

*rjyang@mail.ncku.edu.tw
†wjluo@ncut.edu.tw

Recent theoretical and experimental studies [36,37] have shown that using a three-dimensional (3D) electrode structure, rather than a coplanar electrode structure, can improve the pumping effect induced by an asymmetric electrode array. Urbanski *et al*. [38] conducted an experimental investigation of the effect of the step height on the pumping velocity induced by asymmetric pairs of 3D electrodes and compared the results with those obtained from a simulation model. García-Sánchez *et al*. [39] theoretically demonstrated that the net pumping velocity induced by a TWEO array could be increased by as much as 2.7 times if the electrodes are patterned with a 3D, rather than a two-dimensional (2D), structure. Olesen *et al*. [29] and Ramos *et al*. [40] developed theoretical models to examine the effects of faradic currents on the TWEO phenomena observed in the linear regime. The results obtained from the models were in good qualitative agreement with those obtained from the blocking electrode model. The above literature adopted the linear electro-osmotic model. The nonlinearity may come into play when (1) nonlinear models for the double layer or (2) large voltages are applied to the system. The double layer is considered to be composed of two parts, namely, a Stern layer and a diffuse layer. The electrical behavior of the compact layer can be described as a linear capacitor, with constant capacitance per unit surface C_s. The diffuse layer can be described using the Gouy-Chapman theory as a nonlinear capacitor [41]. Gonzáles *et al*. [42] have analyzed the pumping of electrolytes by TWEO, using a simple nonlinear model of the double layer. For low voltages, the velocity U is proportional to V_0^2, where V_0 is the applied voltage. As the voltage increases, the maximum velocity in the nonlinear regime becomes quasilinear with voltage $U\tilde{V}_0\ln(V_0)$ instead of quadratic. The velocity of the linear solution is faster than that of the nonlinear model. In addition, concentration polarization may become important when the applied voltage is much higher than the thermal voltage k_BT/e. Faradic reactions could be possible without observable electrolysis. Linear and nonlinear models show completely different physical phenomena. For the nonlinear model, faradic reactions, steric effects of the ion, and electro-osmotic instabilities under applied high voltages should be considered.

The many contributions of the studies discussed above investigated the TWEO flow in a microchannel with electrode arrays patterned on only one side of the surface of the channel. The present paper further considers a microchannel containing a double-sided electrode array and examines the dependence of the flow velocity distribution on the relative configuration of the two electrode structures (i.e., symmetrical or staggered), the phase lag between the applied ac signals, and the angular frequency of the signals. The investigation will be analyzed with a linear electro-osmotic model based on the Debye-Hückel theory of the double layer. The potential drop across the diffuse layer is assumed to be less than 25 mV (k_BT/e), and there is a linear response between the surface charge and the voltage drop across the double layer. The double layer is not resolved but is lumped into effective parameters that are imported from the Debye-Hückel and Stern layers. The simulation results provide a useful insight into the optimal design parameters and operating conditions for micropumps containing double-sided microelectrode arrays.

II. MATHEMATICAL ANALYSIS

Figure 1 illustrates the configuration of the two-sided microelectrode array considered in this paper. The simulation model comprises an infinite periodic array of electrodes patterned on an insulating substrate (glass). The electrodes are assumed to be infinitely long and to have a width of d_1 and a spacing of d_2 (see Fig. 2). Four ac signals of amplitude V_0, angular frequency ω, and phases $0°$, $90°$, $180°$, and $270°$ are applied to the array such that the voltage acting on each electrode is phase shifted by $90°$ relative to that acting on its neighbors. A symmetrical electrolyte, for example, KCl, is then injected into the microchannel and is driven toward the outlet via the TWEO effect induced by the electrodes. The electrode array is symmetrical in the transverse direction around the centerline of the microchannel, and a 2D configuration is assumed. In addition, it is assumed that a voltage of 25 mV applied to the electrodes is sufficiently low so that electrolysis does not occur. Finally, the frequency of the applied voltage signal is constrained such that $\ll \sigma/\varepsilon$, where σ and ε, respectively, are the liquid conductivity and the electrical permittivity. Under these conditions, the double layer acts as an ideal capacitor and resides within a quasiequilibrium state.

A. Electrostatics

The electric potential acting on the electrolyte is given by $\phi = \text{Re}[\Phi \exp(i\omega t)]$, where Φ is a phasor satisfying the Laplace equation, i.e.,

$$\nabla^2\Phi = 0. \tag{1}$$

The simulation procedure commences by computing the electric potential distribution throughout the entire domain, and the corresponding electro-osmotic velocity at the electrode surface is then derived. In the present simulations, the effects of the Debye length λ_D were neglected because it is on the order of 10 nm and is negligible compared with the other lengths in the system. The ac electro-osmotic flow distribution is then solved using the Helmholtz-Smoluchowski formula, which accounts for the slip boundary condition at the electrode surface [43].

To describe the charging of the double layer due to the current in the bulk flow, the boundary condition on the electrode surface can be written as $\partial q_s/\partial t = -\sigma(\vec{n}\cdot\vec{\nabla}\Phi)$, where q_s is the charge per unit area in the double layer. If a sufficiently low voltage across the diffuse layer is assumed, then $\Delta\Phi < k_BT/e$, where k_B is the Boltzmann constant, T is the absolute temperature, and e is the charge of an electron. A linear relationship then exists between the surface charge and the voltage drop across the double layer. The resulting polarization of the electrode-electrolyte interface can be modeled by means of the surface impedance Z. The general boundary condition at the electrode surface is then given by

$$\Phi - \sigma Z(\vec{n}\cdot\vec{\nabla}\Phi) = V_j, \tag{2}$$

where $\vec{n}$ is the unit vector normal to the electrode surface and V_j denotes the voltage applied to the jth electrode. The
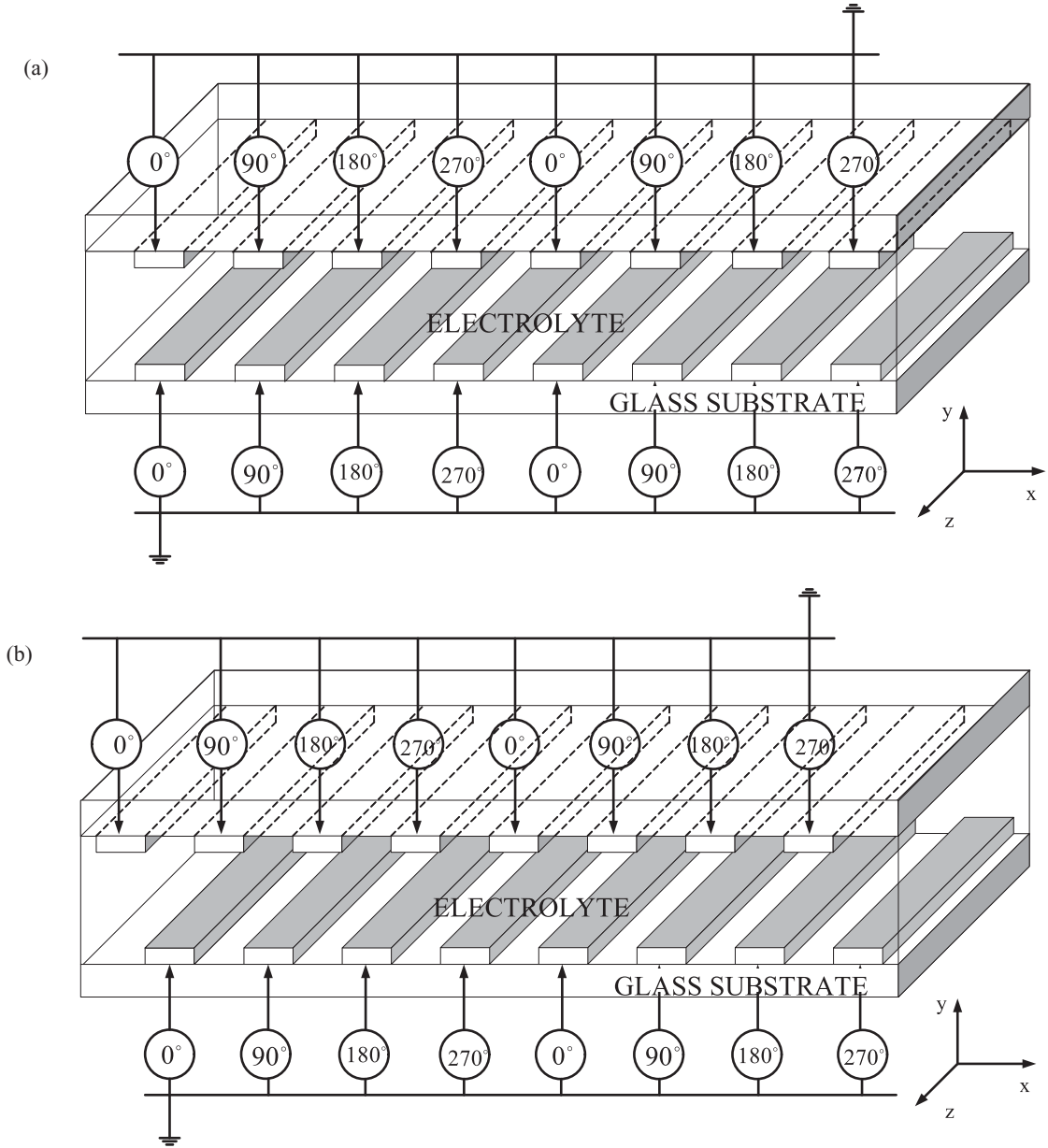
FIG. 1. (a) The symmetrically opposed electrode arrays, (b) the staggered arrangement of the electrode arrays and the relative phase shift applied to the electrodes on the upper and lower walls.

surface impedance Z is modeled using the capacitor model for perfectly blocking electrodes $Z = 1/i\omega C_{DL}$. The parameter $C_D L$ is estimated from Debye-Hückel theory as $C_{DL} = \varepsilon/\lambda_D$, where λ_D is the Debye length and is related to the diffusion coefficient D by $\lambda_D = \sqrt{D\varepsilon/\sigma}$ [44]. These simulations assumed that the faradic currents are reduced to zero, and, thus, the effect of the faradic charge was neglected [43]. A similar boundary condition holds at the interface between the electrolyte and the glass walls of the microchannel. However, the boundary condition can be simplified in this case. In the absence of tangential currents, the total normal current, which includes both free and displacement currents, is continuous,

$$(\sigma + i\varepsilon\omega)\frac{\partial \Phi}{\partial y} = (\sigma_g + i\varepsilon_g\omega)\frac{\partial \Phi_g}{\partial y}, \qquad (3)$$

where σ_g, ε_g, and Φ_g, respectively, are the electrical conductivity, the electrical permittivity, and the electric potential in the glass. Because the conductivity of the glass is negligible and the angular frequency is in the range $\omega \ll \sigma/\varepsilon < \sigma/\varepsilon_g$, the boundary condition on the glass from the liquid side simplifies to $\vec{n} \cdot \vec{\nabla} \Phi = 0$.

B. Fluid dynamics

In the absence of volume forces, the fluid velocity in the microchannel is governed by the Navier-Stokes equations,

$$\frac{\partial u}{\partial x} + \frac{\partial v}{\partial y} = 0, \qquad (4)$$
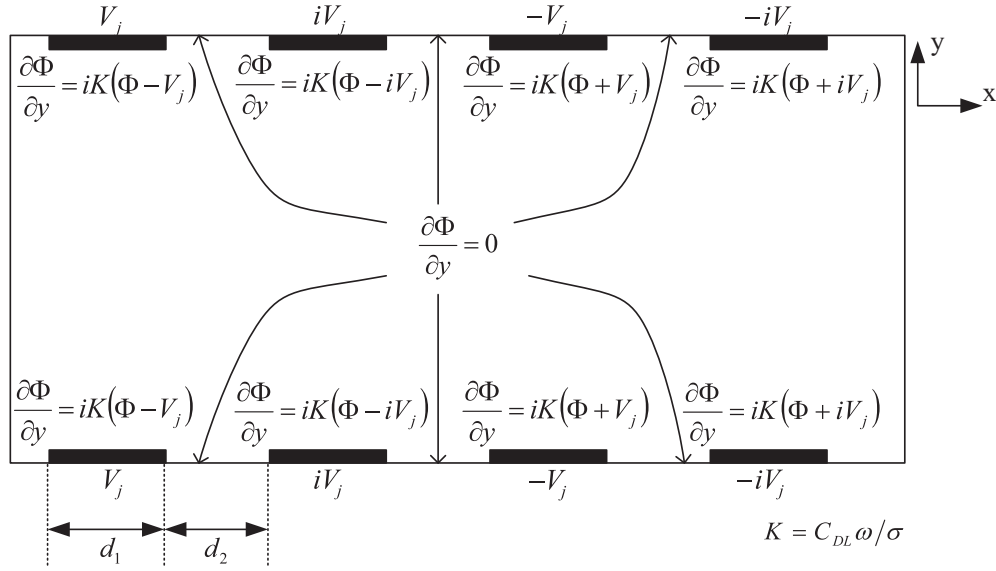
FIG. 2. Boundary conditions of the electric potential for a $0°$ phase shift and symmetrically opposed electrodes.

$$\rho\left(u\frac{\partial u}{\partial x} + v\frac{\partial u}{\partial y}\right) = -\frac{\partial p}{\partial x} + \eta\left(\frac{\partial^2 u}{\partial x^2} + \frac{\partial^2 u}{\partial y^2}\right), \quad (5)$$

$$\rho\left(u\frac{\partial v}{\partial x} + v\frac{\partial v}{\partial y}\right) = -\frac{\partial p}{\partial y} + \eta\left(\frac{\partial^2 v}{\partial x^2} + \frac{\partial^2 v}{\partial y^2}\right), \quad (6)$$

where u and v are the velocity components in the x and y directions, respectively, p is the pressure, and η is the fluid viscosity.

In the present simulations, Eqs. (4)–(6) were solved subject to the following boundary conditions:

(1) In this paper, we simulated the flow field by the Navier-Stokes equations. Since the Reynolds number is less than 1 for most microfluidic systems, the convection term can be neglected in the Navier-Stokes equation. The flow is in the laminar regime.

(2) At the electrode surface, the diffuse double layer is assumed to be in a quasiequilibrium condition, and the electrodes are assumed to have a perfectly polarizable metal surface. Thus, the slip velocity is given by the time-based average of the Helmholtz-Smoluchowski electro-osmotic velocity [45], given by $u_{eo} = \frac{\varepsilon}{\eta}\langle \zeta E_t\rangle$, where ζ is the ζ potential, which is the voltage drop across the diffuse layer at the electrode-electrolyte interface, and E_t is the component of the electric field tangential to the electrode. The time-averaged electro-osmotic velocity can be expressed in terms of the phasor of the electric potential Φ as follows:

$$u_{eo} = -\frac{\varepsilon}{2\eta}\Lambda \text{Re}[(\Phi - V_j)\vec{\nabla}\Phi^* \cdot \vec{t}]$$

$$= -\frac{\varepsilon}{4\eta}\Lambda\frac{\partial}{\partial x}[(\Phi - V_j)(\Phi - V_j)^*], \quad (7)$$

where $*$ indicates the complex conjugate and $\vec{t}$ is a unit vector tangential to the electrode surface. Λ is the ratio of the diffuse double layer impedance to the total double layer impedance, which is given by

$$\Lambda = \frac{(i\omega C_d)^{-1}}{(i\omega C_{DL})^{-1}} = \frac{C_d^{-1}}{C_d^{-1} + C_s^{-1}} = \frac{1}{1 + C_d/C_s}, \quad (8)$$

where C_d and C_s are the capacitances of the diffuse layer and the Stern or compact layer, respectively. The parameter Λ accounts for the fact that only a fraction of the total voltage drop present across the double layer is across the diffuse layer. In this paper, $\Lambda = 0.1$ was chosen following Ref. [34]. While $\Lambda = 1$, the velocity as a function of frequency has a maximum value. The normal velocity at the electrode surface is equal to zero. The boundary conditions of the electric potential for a $0°$ phase shift and symmetrically opposed electrodes are shown in Fig. 2.

(3) At the glass-electrolyte interface, the potential drop across the diffuse double layer is very small and, from Eq. (7), the electro-osmotic velocity on the glass is negligible such that a no-slip condition is imposed.

(4) Periodic boundary conditions are imposed at the left and right boundaries in Fig. 2.

III. RESULTS AND DISCUSSION

The simulations conducted in this paper were performed using the commercial multiphysics software COMSOL (Bandon, MA) based on the finite element method. The 1-mM KCl solution with conductivity $\sigma = 15 \times 10^{-3}\,\text{Sm}^{-1}$ and permittivity $\varepsilon = 80 \times 8.854 \times 10^{-12}\,\text{F/m}$ is used in the simulation. The related dimension values are used as inputs to the software. Then, the computed data are analyzed and are presented in nondimensional form. In the following simulations, the effects of the electrode configuration and the relative phase shift applied to the electrodes were examined for micropumps containing two microelectrode arrays patterned on the upper and lower surfaces of the microchannel. The simulations considered two electrode configurations: one configuration in which the individual electrodes in the lower array were symmetrically opposed to the corresponding electrodes in the upper array, as shown in Fig. 1(a) and a second configuration in which the electrodes in the lower array were staggered relative to those in the upper array, as shown in Fig. 1(b). In the paper, the dimensionless physical quantities of electrode width
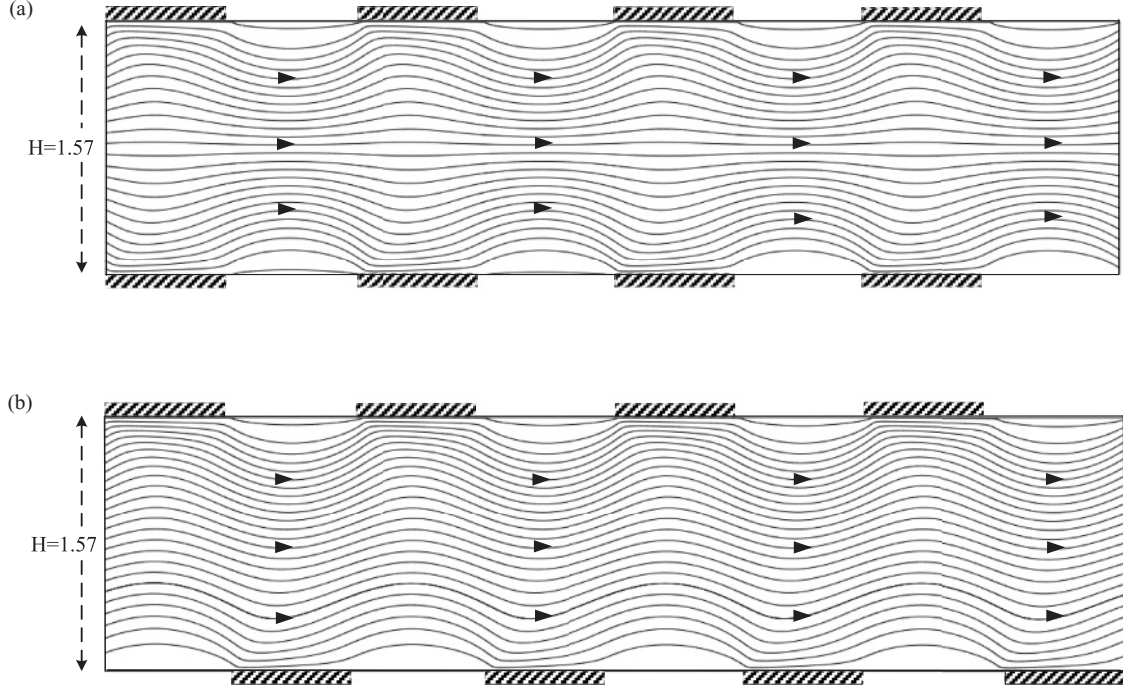
FIG. 3. (a) Net pearl-like streamline distribution of the ac electro-osmotic flow in a microchannel with symmetrically opposed electrodes on the upper and lower microchannel surfaces. (b) The wavelike streamline distribution of the ac electro-osmotic flow in a microchannel with a staggered arrangement of electrodes on the upper and lower surfaces. The applied voltage $V_0^* = 1$ and frequency $\Omega = 1$.

D_1, electrode spacing D_2, microchannel height H, pumping velocity U, flow rate Q, angular frequency of the potential signal Ω, and electric potential were defined as follows:

$$D_1 = k_0 d_1, \quad D_2 = k_0 d_2, \quad H = k_0 h, \quad U = \frac{2u_p \eta}{\Lambda \varepsilon k_0 V_0^2},$$

$$Q = \frac{q}{\Lambda \varepsilon V_0^2 / 4\eta}, \quad \Omega = \frac{\omega \varepsilon L}{2\pi \sigma \lambda_D}, \quad \phi^* = \frac{\phi e}{k_B T},$$

$$\text{and} \quad V_0^* = \frac{V_0 e}{k_B T},$$

where $k_0 = \frac{2\pi}{L}$, $L = 4(d_1 + d_2)$, q is the flow rate computed from the equation $q = \int_0^h u\, dy$, and h is the height of the microchannel. The parameter u_p is the pumping velocity, which is defined as $u_p = \frac{1}{L} \int_0^L u_{eo}\, dx$, and u_{eo} is the streamwise time-averaged velocity on the electrodes. In this paper, V_0 is the applied voltage with a value of 25 mV on the electrodes. L is the characteristic length of electrode 80 μm.

A. The induced ac electro-osmotic flow within the microchannels that contain a symmetrical or a staggered electrode arrangement

The electrode width and electrode spacing were specified in the simulations as $D_1 = D_2 = 0.785$ for both microelectrode arrays. Four sinusoidal ac signals with a phase shift of $\pi/2$ between successive electrodes were applied to every four electrodes in each array to create a traveling-wave potential. The amplitude and frequency of the ac signal applied to each electrode were $V_0^* = 1$ and $\Omega = 1$, respectively. Figure 3(a) illustrates the pearl-like streamline distribution of the ac electro-osmotic flow induced in the microchannel with a dimensionless height of 1.57 and a symmetrical arrangement of the two electrode structures. Figure 3(b) shows the wavelike streamline distribution of the ac electro-osmotic flow induced in the same microchannel but with a staggered arrangement of the electrodes on the upper and lower surfaces. Due to the induced pumping velocity above the electrodes and the viscous friction on the glass surfaces, the streamlines within the microchannels were gathered toward the electrode surfaces and were distanced from the glass surfaces, respectively. These effects caused the pearl-like streamline distribution and the wavelike streamline distribution shown in the two figures. The flow patterns in the microchannels with symmetrical or staggered arrangements of electrodes were independent of the relative phase shift of the potential signals applied to the opposed electrodes on the upper and lower walls. Figure 4 illustrates the variation of the pumping velocity with increasing microchannel height for the cases shown in Figs. 1 and 1(b). In both cases, it was found that, for a microchannel height of $H > 5$, the pumping velocity above the electrodes almost remained constant with the increase in the microchannel height. In both cases, this result indicates that the interaction effect between the electrode arrays on the upper and lower surfaces became very weak when the microchannel height was $H > 5$. However, for a microchannel height of $H < 5$, the pumping velocity obtained in the two microchannels gradually increased in proportion to the microchannel height when $H < 0.98$ and decreased in inverse proportion to the microchannel height when $0.98 < H < 5$. It was found that the pumping velocity was higher than that in a microchannel with a single set of electrodes on the wall. As an example, Fig. 5 shows the pumping velocity versus angular frequency for the case of $H = 1.57$ under a phase shift of zero with different electrode
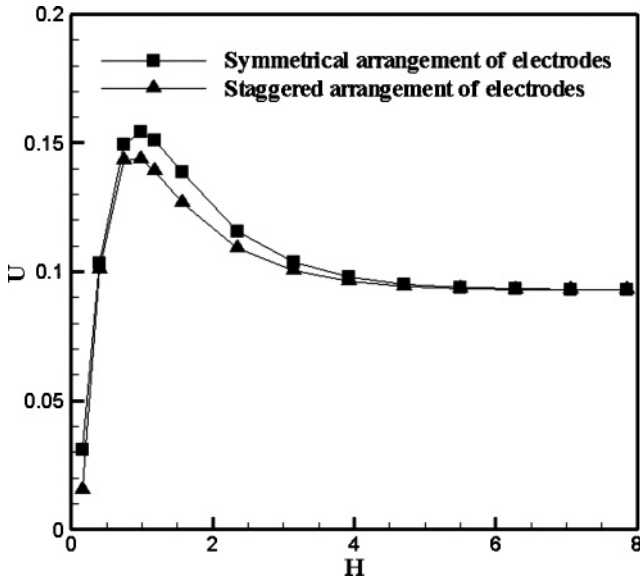
FIG. 4. The variation of the pumping velocity at different microchannel heights. The applied voltage $V_0^* = 1$ and frequency $\Omega = 1$.

configurations. When $\Omega = 1$, the maximum pumping velocity with symmetrically opposed electrodes was found to be 2.7 times higher than the maximum pumping velocity with a single set of electrodes. Similarly, the maximum pumping velocity with a staggered arrangement of electrodes was found to be 2.4 times higher than the maximum pumping velocity with a single set of electrodes. Although a closer alignment of electrodes can exert a stronger electro-osmotic effect, the narrower channel height also augments the viscous forces within the fluid. Due to these two counteractive influences, there exists an optimal microchannel height of about $H = 0.98$ such that the pumping velocity is maximized.
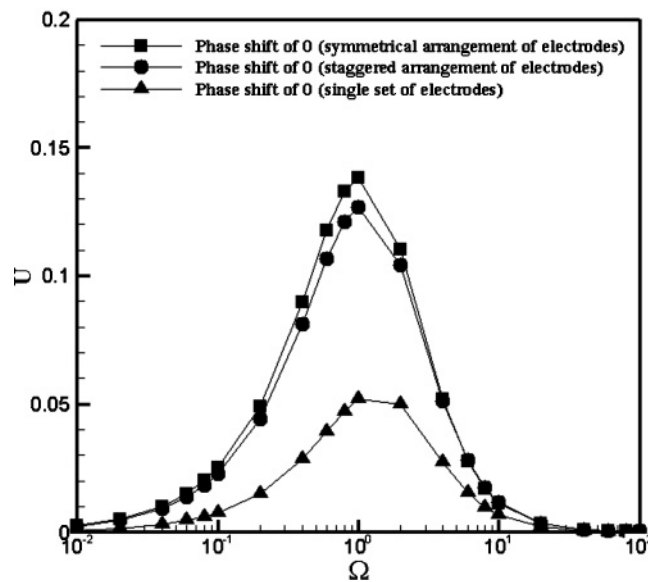

FIG. 5. The pumping velocity versus angular frequency for different electrode configurations. The applied voltage $V_0^* = 1$ and channel height $H = 1.57$.

B. The pumping velocity above the electrode induced by the applied signals with various phase shifts

The pumping velocity within the microchannel is determined not only by the relative positions of the electrodes on the upper and lower surfaces, but also by the relative phase shift of the potential signals applied to the symmetrically opposed electrode and the electrode of staggered arrangement. According to Eq. (7), the derivative of $|\phi^* - V_0^*|^2$ with respect to x gives the slip velocity on each electrode. Figures 6(a) and 6(b) show the function of $|\phi^* - V_0^*|^2$ and pumping velocity along the surface of a single electrode at the lower side for the cases with symmetrically opposed electrodes and electrodes in the staggered arrangement, where $V_0^* = 1$, $D_1 = 0.785$, and $\Omega = 1$. The maximum induced pumping velocity could be reached around $\Omega = 1$ to 2. Although the values of $|\phi^* - V_0^*|^2$ in the case of the phase shift of $3\pi/2$ for the symmetric case and π for the staggered case were higher than those in the other cases, their derivatives of $|\phi^* - V_0^*|^2$ were not the greatest among the cases. According to Eq. (7), the difference in the values of $|\phi^* - V_0^*|^2$ at the edges gives the pumping velocity. The directions of the induced flows over the electrode are from left to right. As shown in Fig. 6(a), with phase shifts of zero and $3\pi/2$, the slope of $|\phi^* - V_0^*|^2$ is much greater than that in the cases with phase shifts of $\pi/2$ and π. Therefore, the maximum pumping velocity within the microchannel was obtained while the potential signals applied to the symmetrically opposed electrode had a phase shift of zero or $3\pi/2$. On the contrary, the minimum pumping velocity within the microchannel was obtained when the potential signals applied to the symmetrically opposed electrode had a phase shift of $\pi/2$ or π. As shown in Fig. 6(b), with a phase shift of $3\pi/2$, the slope of $|\phi^* - V_0^*|^2$ was much greater than those of the cases with a phase shift of zero, $\pi/2$, and π. Therefore, the maximum pumping velocity within the microchannel was obtained when the potential signals applied to the electrodes in the staggered arrangement had a phase shift of $3\pi/2$. On the contrary, the minimum pumping velocity within the microchannel was obtained when the potential signals applied to the electrode in the staggered arrangement had a phase shift of $\pi/2$.

C. The effect of the angular frequency on the pumping velocity

Figure 7(a) shows the pumping velocity versus the angular frequency Ω for the cases in which the potentials applied to the symmetrically opposed electrodes had phase shifts of 0, $\pi/2$, π, and $3\pi/2$. In the figure, for the case of an identical phase shift, the induced pumping velocity was able to reach its maximum value $U = 0.138$ at $\Omega = 1$. For the cases with phase shifts of $\pi/2$ and $3\pi/2$, due to similar electric potential distributions, the induced pumping velocity could reach the same maximum value of about 0.091 at $\Omega = 1$. However, for the case of a phase shift of π, the maximum pumping velocity could be reached at $\Omega = 2$ and was the smallest among the maximum velocity values for the cases with different phase shifts. The corresponding angular frequency relative to the maximum pumping velocity was determined by the characteristic charging time of the RC equivalent circuit in the system. Due to the same polarity of the electrical signals applied to the symmetrically opposed
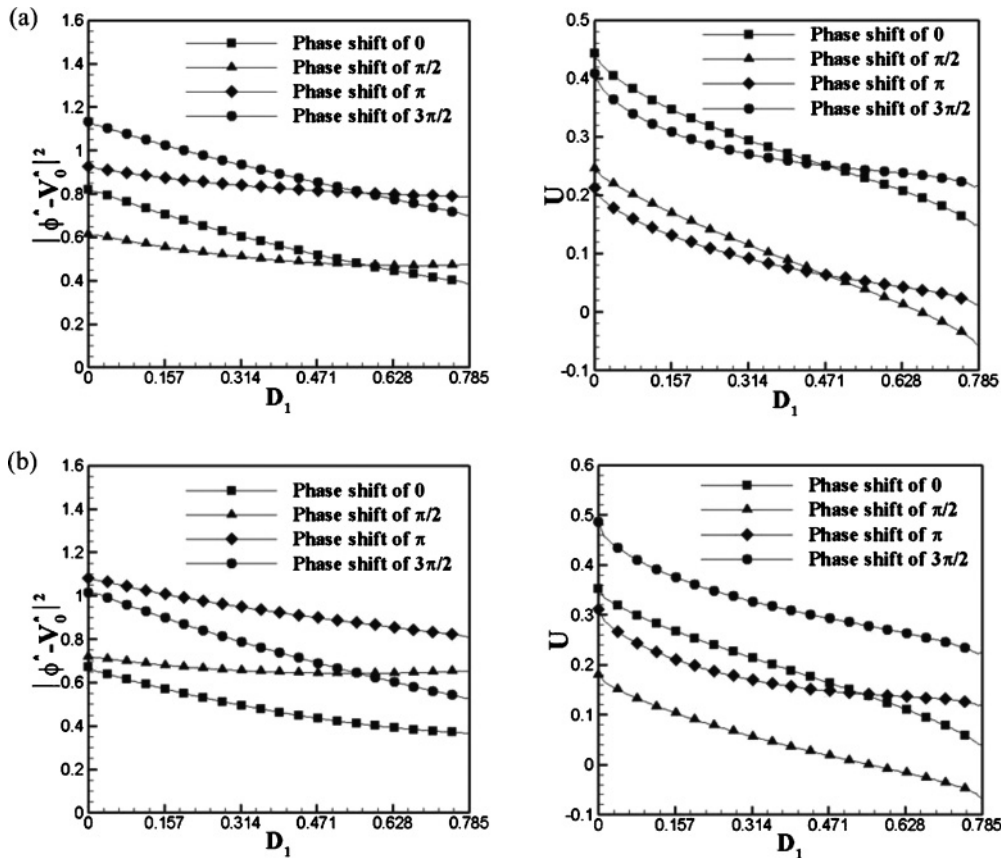
FIG. 6. The function $|\phi^* - V_0^*|^2$ and the pumping velocity on top of the electrodes for $0°$, $90°$, $180°$, and $270°$ phase shifts with (a) symmetrically opposed electrodes and (b) staggered arrangement of the electrodes. The applied voltage $V_0^* = 1$, frequency $\Omega = 1$, and channel height $H = 1.57$.

electrodes, the saturated concentration of the counterions accumulating within the double layer was greatest for the case with an identical phase shift. The value of the capacitance in the RC equivalent circuit was the largest among the four cases shown in Fig. 7(a), and the longest charging time was required to reach the saturation state of ions within the double layer. Consequently, the corresponding angular frequency relative to the maximum pumping velocity was the lowest among the four cases. In comparison to the case with a phase shift of π, the saturated concentration of the counterions accumulating within the double layer was the smallest due to the opposite polarity of the potential signals applied to the symmetrically opposed electrodes. A shorter charging time was necessary to reach ion saturation within the double layer. Consequently, the corresponding angular frequency relative to the maximum pumping velocity was the highest among the four cases. For the case in which the applied angular frequency was higher than the angular frequency that corresponded to the maximum pumping velocity, the ion concentration that accumulated within the electric double layer was less than the saturated concentration due to a shorter charging time. Consequently, the pumping velocity was also less than the maximum pumping velocity. When the applied angular frequency was less than the angular frequency corresponding to the maximum pumping velocity, the ions within the electric double layer were driven to move downward, but the polarity

of the applied electrical signals on the electrodes could not change in time. The ion concentration within the electric double layer was never replenished by the other counterions in the bulk flow. Consequently, the pumping velocity above the electrodes was also less than the maximum pumping velocity.

Figure 7(b) shows the pumping velocity versus the dimensionless angular frequency Ω for the cases in which the potentials applied to staggered electrodes had phase shifts of 0, $\pi/2$, π, and $3\pi/2$. Because the electric potential distributions for the two cases with phase shifts of 0 and $3\pi/2$ were symmetrical to the centerline of the microchannel, the induced pumping velocities could both reach their maximum values of $U = 0.126$ at $\Omega = 1$. For the other two cases with phase shifts of $\pi/2$ and π, their electric potential distributions were also symmetrical to the centerline of the microchannel, and the induced pumping velocities both could reach the same maximum values of $U = 0.058$ at $\Omega = 2$. For the two cases with phase shifts of 0 and $3\pi/2$, the saturated concentration of the counterions that accumulated within the double layer was higher in comparison to the two cases with phase shifts of $\pi/2$ and π. As a result, the value of the capacitance in the RC equivalent circuit was greater for the two cases with phase shifts of 0 and $3\pi/2$, and a longer charging time was required to achieve ion saturation within the double layer. This phenomenon resulted in a lower angular frequency relative to
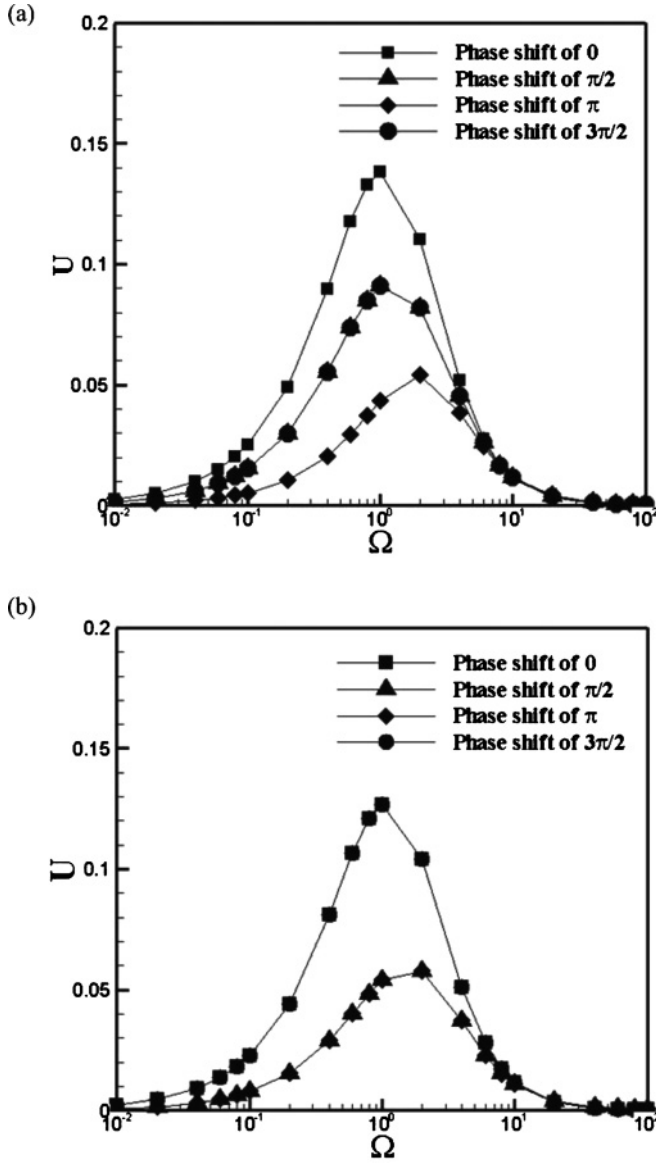
(a)

(b)

FIG. 7. (a) Pumping velocity versus angular frequency for the microchannel with symmetrically positioned electrodes. (b) Pumping velocity versus angular frequency for the microchannel with a staggered arrangement of electrodes. The applied voltage $V_0^* = 1$ and channel height $H = 1.57$.

that of the maximum pumping velocity in comparison to the two cases with phase shifts of $\pi/2$ and π.

D. The flow rates at the outlet induced by the applied signals with various phase shifts

Table I illustrates the flow rates calculated at the outlets of two microchannels containing symmetrical and staggered electrode microstructures for four different values of the potential phase shift at $\Omega = 1$. For both electrode arrangements, the maximum flow rate was obtained when the potentials applied to the electrodes in the upper and lower arrays had a phase shift of zero. For the symmetric electrode configuration, the flow rate had a maximum value of 0.43. In addition, the dimensionless flow rate obtained for a phase shift of $\pi/2$ or

TABLE I. Flow rates (Q) at the outlets of microchannels with symmetrically positioned electrodes and the staggered arrangement of electrodes as a function of the phase shift in the applied potential signals.

Phase shift	Symmetrical arrangement of electrodes	Staggered arrangement of electrodes
0	0.43	0.40
$3\pi/2$	0.28	0.17
π	0.14	0.17
$3\pi/2$	0.28	0.40

$3\pi/2$ was 0.28 in both cases. The electrical field has the same potential distribution but in reversed form for both phase shifts $\pi/2$ and $3\pi/2$. Therefore, these two cases produce equal flow rates. Meanwhile, the minimum dimensionless flow rate $Q = 0.14$ was obtained for a phase shift of π. For the microchannel with a staggered electrode configuration, the electric potential distributions are identical for the two cases with phase shifts of 0 and $3\pi/2$. Consequently, the maximum dimensionless flow rate was found to be 0.40 and was obtained due to the equal polarity of the relative electrode arrays on the upper and lower surfaces. Finally, for the other two cases with phase shifts of $\pi/2$ and π symmetrical to the centerline of the microchannel, the minimum dimensionless flow rate $Q = 0.17$ was obtained for a phase shift of either $\pi/2$ or π due to the opposite polarity of the relative electrode arrays on the upper and lower surfaces. The corresponding flow rates are equal for either case of phase shifts 0 and $3\pi/2$ or $\pi/2$ and π due to the fact that they have same potential distributions but in reversed form.

IV. CONCLUSIONS

In this paper, a series of numerical simulations was carried out to investigate the pumping performance of micropumps containing two electrode arrays patterned on the upper and lower surfaces of the microchannel. The effect of the microchannel height on the pumping velocity was investigated for symmetrical and staggered arrangements of the electrode arrays on the upper and lower surfaces. When the microchannel height was less than the critical value, the interaction of the applied electrical potentials from the upper and lower surfaces became significant and could either enhance or suppress the induced pumping velocity above the electrodes, depending on the relative phase shift of the potential signals applied to the electrodes. The electrode configuration and the relative phase shift applied to the electrodes while the microchannel height was below the critical value both represent factors that can affect the pumping performance.

For the micropump containing a symmetrical arrangement of the electrode arrays on the upper and lower surfaces, the maximum pumping effect was obtained when the potential signals applied to the equivalent electrodes in the two arrays had a zero phase shift. In contrast, a phase shift of π yielded the poorest pumping performance due to the opposite polarity of the potential signals applied to the equivalent electrodes. For the staggered case, the maximum flow rate was obtained with the phase shift of zero and $3\pi/2$ and the minimum flow

rate was obtained with the phase shift of $\pi/2$ and π. In general, the induced pumping velocity for the staggered case is a little bit lower than that of the symmetrical case. The effect of the applied angular frequency on the pumping velocity was also investigated. Our results indicate that the micropump with a symmetrical microelectrode configuration and a zero phase shift yielded an improved pumping performance with an applied angular frequency of $\Omega = 1$. Finally, the flow rate of the micropump also could be controlled by varying the phase shift of the applied potentials on the upper and lower electrodes.

[1] H. Stone, A. Stroock, and A. Ajdari, Annu. Rev. Fluid Mech. **36**, 381 (2004).

[2] Q. Cui, C. Liu, and X. F. Zha, Microfluid. Nanofluid. **3**, 377 (2007).

[3] Y. S. Kim, J. H. Kim, K. H. Na, and K. Rhee, Proc. Inst. Mech. Eng., Part C: J. Mech. Eng. Sci. **219**, 1139 (2005).

[4] A. Geipel, A. Doll, P. Jantscheff, N. Esser, U. Massing, P. Woias, and F. Goldschmidtboeing, J. Micromech. Microeng. **17**, 949 (2007).

[5] J. Goulpeau, D. Trouchet, A. Ajdari, and P. Tabeling, J. Appl. Phys. **98**, 044914 (2005).

[6] S.-Y. Yang, S.-K. Hsiung, Y.-C. Hung, C.-M. Chang, T.-L. Liao, and G.-B. Lee, Meas. Sci. Technol. **17**, 2001 (2006).

[7] K.-F. Lei, W.-C. Law, Y.-K. Suen, W.-J. Li, Y. Yam, H.-P. Ho, and S.-K. Kong, Proc. Inst. Mech. Eng., Part H: J. Eng. Med. **221**, 129 (2007).

[8] S. Maruo and H. Inoue, Appl. Phys. Lett. **89**, 144101 (2006).

[9] M. Matteucci, F. Perennes, B. Marmiroli, P. Miotti, L. Vaccari, A. Gosparini, A. Turchet, and Di Fabrizio, Microelectr. Eng. **83**, 1288 (2006).

[10] A. Manz, C. S. Effenhauser, N. Burggraf, D. J. Harrison, K. Seiler, and K. Fluri, J. Micromech. Microeng. **4**, 257 (1994).

[11] G. Beni and M. Tenan, J. Appl. Phys. **52**, 6011 (1995).

[12] D. E. Kataoka and S. M. Troian, Nature (London) **402**, 794 (1999).

[13] G. Fuhr, R. Hagedorn, T. Muller, W. Benecke, and B. Wagner, J. Microelectromech. Syst. **1**, 141 (1992).

[14] N. G. Green, A. Ramos, A. González, H. Morgan, and A. Castellanos, Phys. Rev. E **61**, 4011 (2000).

[15] A. Ramos, H. Morgan, N. Green, and A. Castellanos, J. Colloid Interface Sci. **217**, 420 (1999).

[16] A. González, A. Ramos, N. G. Green, A. Castellanos, and H. Morgan, Phys. Rev. E **61**, 4019 (2000).

[17] A. Ajdari, Phys. Rev. E **61**, 45 (2000).

[18] V. Studer, A. Pépin, Y. Chen, and A. Ajdari, Microelectron Eng. **61–62**, 915 (2002).

[19] M. Mpholo, C. G. Smith, and A. B. D. Brown, Sens. Actuators B **92**, 262 (2003).

[20] D. Lastochkin, R. Zhou, P. Whang, Y. Ben, and H. C. Chang, J. Appl. Phys. **96**, 1730 (2004).

[21] S. Debesset, C. J. Hayden, C. Dalton, J. C. T. Eijkel, and A. Manz, Lab Chip **4**, 396 (2004).

[22] V. Studer, A. Pépin, Y. Chen, and A. Ajdari, Analyst (Cambridge, UK) **129**, 944 (2004).

[23] B. P. Cahill, L. J. Heyderman, J. Gobrecht, and A. Stemmer, Phys. Rev. E **70**, 036305 (2004).

[24] A. Ramos, H. Morgan, N. G. Green, A. González, and A. Castellanos, J. Appl. Phys. **97**, 084906 (2005).

[25] P. García-Sánchez, A. Ramos, N. G. Green, and H. Morgan, IEEE Trans. Dielectr. Electr. Insul. **13**, 670 (2006).

[26] A. B. D. Brown, C. G. Smith, and A. R. Rennie, Phys. Rev. E **63**, 016305 (2000).

[27] A. Ramos, A. González, A. Castellanos, N. G. Green, and H. Morgan, Phys. Rev. E **67**, 056302 (2003).

[28] N. A. Mortensen, L. H. Olesen, L. Belmon, and H. Bruus, Phys. Rev. E **71**, 056306 (2005).

[29] L. H. Olesen, H. Bruus, and A. Ajdari, Phys. Rev. E **73**, 056313 (2006).

[30] L. Olesen, Ph.D. thesis, Technical University of Denmark, 2006.

[31] A. Ramos, H. Morgan, N. G. Green, and A. Castellanos, J. Phys. D **31**, 2388 (1998).

[32] A. Castellanos, A. Ramos, A. González, N. G. Green, and H. Morgan, J. Phys. D **36**, 2584 (2003).

[33] H. Morgan, A. García, D. Bakewell, N. G. Green, and A. Ramos, J. Phys. D **34**, 1553 (2001).

[34] N. G. Green, A. Ramos, A. González, H. Morgan, and A. Castellanos, Phys. Rev. E **66**, 026305 (2002).

[35] L. Cui, D. Holmes, and H. Morgan, Electrophoresis **22**, 3893 (2001).

[36] M. Z. Bazant and Y. Ben, Lab Chip **6**, 1455 (2006).

[37] J. P. Urbanski, T. Thorsen, J. Levitan, and M. Z. Bazant, Appl. Phys. Lett. **89**, 143508 (2006).

[38] J. P. Urbanski, J. A. Levitan, D. N. Burch, T. Thorsen, and M. Z. Bazant, J. Colloid Interface Sci. **309**, 332 (2007).

[39] P. García-Sánchez and A. Ramos, Microfluid. Nanofluid. **5**, 307 (2008).

[40] A. Ramos, A. González, P. García-Sánchez, and A. Castellanos, J. Colloid Interface Sci. **309**, 323 (2007).

[41] R. Hunter, *Zeta Potential in Colloid Science* (Academic, San Diego, 1981).

[42] A. González, A. Ramos, and A. Castellanos, Microfluid. Nanofluid. **5**, 507 (2008).

[43] N. G. Green, A. Ramos, and H. Morgan, J. Electrost. **56**, 235 (2002).

[44] R. Hunter, *Introduction to Modern Colloid Science* (Oxford University Press, Oxford, 1993).

[45] A. Bard and L. Faulkner, *Electrochemical Methods: Fundamentals and Applications* (Wiley, New York, 2001).